Volume 10
Number 26
14 July 2022
Pages 4899–5096

Journal of
Materials Chemistry B

Materials for biology and medicine

rsc.li/materials-b

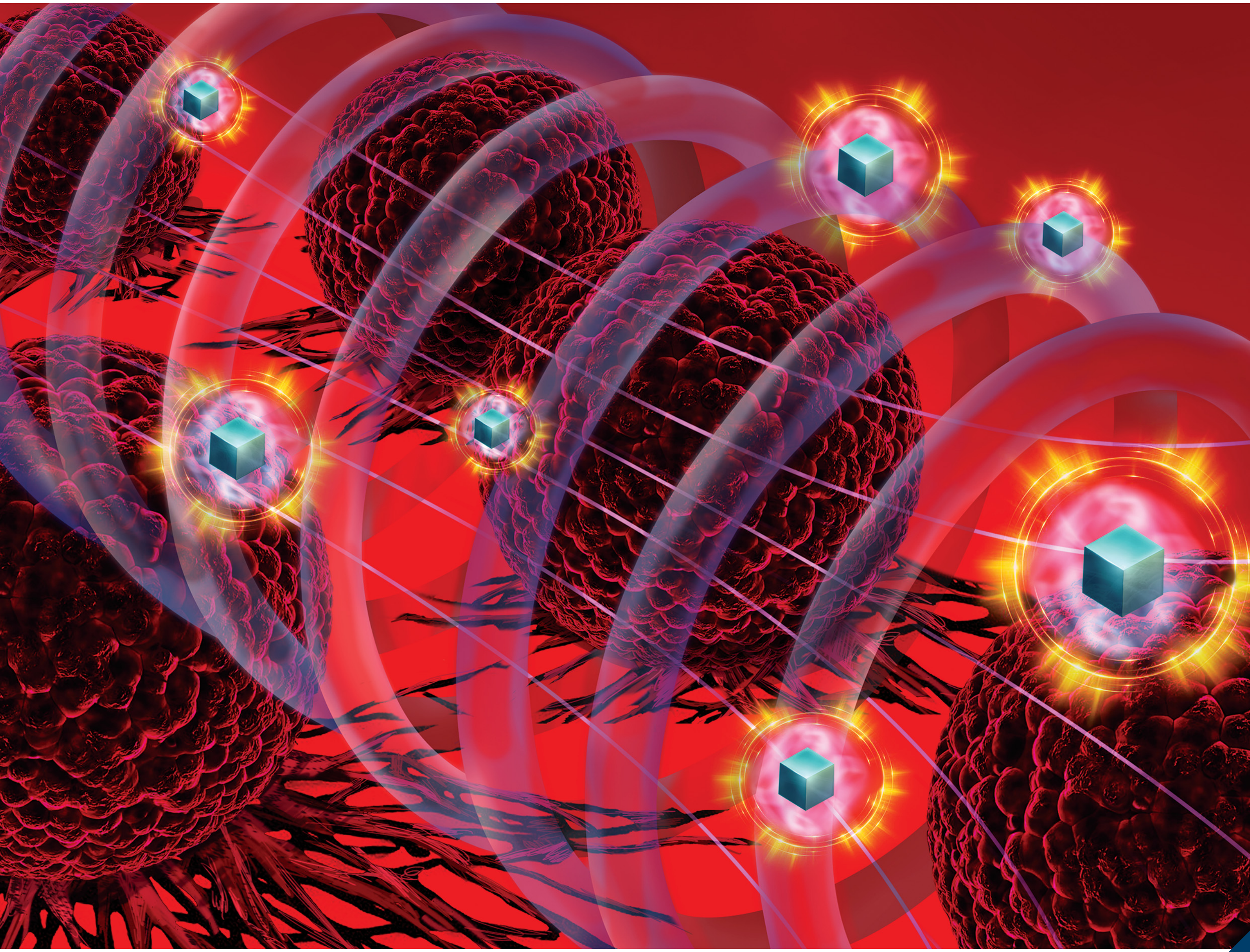

ISSN 2050-750X

ROYAL SOCIETY
OF CHEMISTRY

PAPER

Georgia Basina, Constantinos Hadjipanayis,
Vasileios Tzitzios *et al.*

LAPONITE® nanodisk-“decorated” Fe_3O_4 nanoparticles:
a biocompatible nano-hybrid with ultrafast magnetic
hyperthermia and MRI contrast agent ability

Journal of
Materials Chemistry B

PAPER

View Article Online
View Journal | View Issue

Check for updates

Cite this: *J. Mater. Chem. B*, 2022, **10**, 4935

LAPONITE® nanodisk-"decorated" Fe_3O_4 nanoparticles: a biocompatible nano-hybrid with ultrafast magnetic hyperthermia and MRI contrast agent ability†

Georgia Basina, *[a,b] George Diamantopoulos, [b] Eamonn Devlin, [b] Vassilis Psycharis, [b] Saeed M. Alhassan, [c] Michael Pissas, [b] George Hadjipanayis, [a] Aphrodite Tomou, [b,d] Alexandros Bouras,[e] Constantinos Hadjipanayis *[e] and Vasileios Tzitzios *[b,c]

Received 17th January 2022,
Accepted 25th April 2022

DOI: 10.1039/d2tb00139j

rsc.li/materials-b

Magnetic Fe_3O_4 nanoparticles "decorated" by LAPONITE® nanodisks have been materialized utilizing the Schikorr reaction following a facile approach and tested as mediators of heat for localized magnetic hyperthermia (MH) and as magnetic resonance imaging (MRI) agents. The synthetic protocol involves the interaction between two layered inorganic compounds, ferrous hydroxide, $Fe(OH)_2$, and the synthetic smectite LAPONITE® clay $Na_{0.7}^{+}[(Si_8Mg_{5.5}Li_{0.3})O_{20}(OH)_4]_{0.7}^{-}$, towards the formation of superparamagnetic Fe_3O_4 nanoparticles, which are well decorated by the diamagnetic clay nanodisks. The latter imparts high negative ζ-potential values (up to −34.1 mV) to the particles, which provide stability against flocculation and precipitation, resulting in stable water dispersions. The obtained LAPONITE®-"decorated" Fe_3O_4 nanohybrids were characterized by powder X-ray diffraction (XRD), transmission electron microscopy (TEM), Mössbauer spectroscopy, dynamic light scattering (DLS) and vibrating sample magnetometry (VSM) at room temperature, revealing superior magnetic hyperthermia performance with specific absorption rate (SAR) values reaching 540 W g_{Fe}^{-1} (28 kA m^{-1}, 150 kHz) for the hybrid material with a magnetic loading of 50 wt% Fe_3O_4/LAPONITE®. Toxicity studies were also performed with human glioblastoma (GBM) cells and human foreskin fibroblasts (HFF), which show negligible to no toxicity. Furthermore, T_2-weighted MR imaging of rodent brain shows that the LAPONITE®-"decorated" Fe_3O_4 nanohybrids predominantly affected the transverse T_2 relaxation time of tissue water, which resulted in a signal drop on the MRI T_2-weighted imaging, allowing for imaging of the magnetic nanoparticles.

Introduction

In 1930, J. Frenkel and J. Doefman[1] envisioned spontaneous and induced magnetism in ferromagnetic bodies with the existence of critical domain size, with smaller particles exhibiting a single magnetic domain, where the magnetic moments of free electrons are parallelly aligned. There is an ever-increasing interest in the scientific community for the development and study of magnetic materials in the small nanoscale regime.[2–4] This interest is mainly due to the growing

---

[a] Department of Physics and Astronomy, University of Delaware, Newark, DE 19711, USA. E-mail: g.basina@inn.demokritos.gr
[b] Institute of Nanoscience and Nanotechnology, NCSR Demokritos, 15310, Athens, Greece. E-mail: v.tzitzios@inn.demokritos.gr
[c] Department of Chemical Engineering, Khalifa University, P.O. Box 127788, Abu Dhabi, United Arab Emirates
[d] Goodfellow Cambridge Ltd., Ermine Business Park, Huntingdon PE29 6WR, Cambridge, UK
[e] Brain Tumor Nanotechnology Laboratory, Department of Neurosurgery, Icahn School of Medicine at Mount Sinai, New York, NY, USA.
E-mail: Constantinos.Hadjipanayis@mountsinai.org

† Electronic supplementary information (ESI) available: Structural, magnetic, and morphological characterization data based on XRD, VSM, TEM analysis of various LAPONITE®-"decorated" Fe_3O_4 nanoparticle hybrids with 25 to 95 wt% magnetic content. Summarized hydrodynamic diameter and ζ-potential distribution histograms are also provided for the physicochemical characterization analysis of the prepared Fe_3O_4/LAPONITE® hybrids. AFM images of the selected 50 wt% Fe_3O_4/LAPONITE® are presented. Finally, the temperature profile as a function of the field exposure time from various concentrations (5.5–22 mg mL^{-1}) of colloidal solutions of 25, 50, and 75 wt% Fe_3O_4/LAPONITE® hybrids and a literature review on SAR values as a function of the applied field frequency and strength of Fe-oxide based nanomaterials with various sizes and morphologies are given for comparison. See DOI: **https://doi.org/10.1039/d2tb00139j**

exploration of new magnetic properties for their use in applied magnetism and related device technologies as well as their utilization in commercially available future emerging technologies.[5–7]

Amongst the various magnetic materials, the ferrimagnetic magnetite (Fe_3O_4) is the most extensively studied material in the field of biomedicine,[6,8–12] involving magnetic resonance imaging (MRI),[13–18] magnetic hyperthermia,[19–24] drug delivery[25–28] and biomolecular separation.[9,29] Magnetite has been involved in clinical use for many decades, demonstrating its safety, utility and versatility and is among the few, if not the only, nanomaterials that are FDA approved for *in vivo* applications.[30] It also continues to emerge as one of the most powerful nanomaterials for other technological[10] and environmental applications,[31] including arsenic removal from drinking water in both arsenate and arsenite forms[32,33] or other magnetic separation technologies[34–37] and catalysis.[38–40]

In the last few decades, a plethora of works have been published on the development of protocols, following both physical and chemical approaches for the synthesis of magnetite (Fe_3O_4) nanoparticles.[41] The most popular are those involving chemical synthesis in solutions due to their ability to precisely control the size and the shape of the particles at the nanometer scale. These include the traditional co-precipitation, polyol, thermal decomposition and organometallic approaches.[10,12,13,17,26,41–44]

The application of heat as a theranostic methodology has a long history. It firstly appeared in ancient Greeks', Romans', and Egyptians' findings who utilized heat to treat breast masses.[45] Afterwards, magnetic hyperthermia, again, was at the forefront of the research in the 1950's when it was applied for the selective inductive heating of the lymph nodes,[46] nevertheless it was only approved for phase II clinical trials in the treatment of human cancer patients in 2011.[24] Magnetic hyperthermia studies the rate at which the energy is absorbed per unit mass by a human body when it is exposed to a radio frequency (RF) electromagnetic field. This is achieved by the specific absorption rate (SAR); a quantity that is highly dependent on the applied magnetic field frequency and strength, as well as the type and the concentration of magnetic nanoparticles (MNPs). The use of MNPs has been proven to be extremely efficient in achieving high SAR values. In the case of magnetite, the vast majority of the literature reports that there is an optimal size in the range of 15 to 20 nm for individual Fe_3O_4 nanoparticles in order to achieve the maximum SAR value.[8,21,47] Recently, it has been shown that the formation of nano-assemblies using individual superparamagnetic Fe_3O_4 nanoparticles as building blocks significantly increases the heating performance.[14,22,23,48] It is also worth mentioning that the morphology in terms of particle shape is very influential and can significantly affect hyperthermia efficacy.[23,49–51] Fe_3O_4 nanocubes and nanorods are among the most efficient morphologies for magnetic hyperthermia, revealing SAR values up to 1045 W $g_{Fe}{}^{-1}$.[51] In addition, the heating efficacy depends to a large extent on the frequency and amplitude of the magnetic field. The frequency dependence on the produced power is almost linear in a wide frequency range.[52] However, there are limits of human exposure for both, with the recommended frequency proposed to be about 200 kHz or lower.[53] Selected data associated with the morphology and size effects combined with hyperthermia conditions (magnetic field and frequency) in relation to the SAR values, and therefore magnetic hyperthermia performance, are summarized in Table S1 in the ESI.†

Fe_3O_4 hybrid platforms, in terms of surface functionalization and fabrication of composite materials, have been extensively studied for both imaging and therapy biomedical applications.[12] Lately, two-dimensional materials and their corresponding magnetic composites have attracted enormous interest due to their unique morphological, electronic, and physicochemical properties.[54,55] Fe_3O_4 graphene oxide hybrids are among the most studied for magnetic hyperthermia, with a high SAR value of 543 W g^{-1} at 325 kHz and an amplified magnitude field (AMF) value of 16.72 kA m^{-1},[56] as well as drug delivery and imaging.[57] Furthermore, layered double hydroxide, (LDH), Fe_3O_4 nanohybrids were also reported due to their negligible toxicity as excellent candidates for biomedical applications, including drug delivery and therapy.[58,59] The LAPONITE®/iron oxide nanocomposites have been studied for bioseparation,[60] pH, and thermosensitive drug release,[61–63] and T_2-weighted MR contrast agents.[64,65]

In this study, we report a large scale (up to 1 L, 10 mg mL^{-1}) ferrofluid synthesis based on LAPONITE®-"decorated" Fe_3O_4 hybrid nanomaterials, which demonstrate outstanding stability in water, and superparamagnetic behavior, together with excellent cytotoxicity behavior and magnetic hyperthermia performance at a very low frequency (150 kHz). MR imaging of the LAPONITE®-"decorated" Fe_3O_4 nanoparticles was performed after convection-enhanced delivery (CED) of the nanoparticles into the rodent brain.

Results and discussion

A facile, versatile, and scalable approach to the development of ultra-stable magnetic iron-based hydrosols is herein described. The methodology is based on the interaction between the positively charged layered ferrous hydroxide, $Fe(OH)_2$, with the negatively charged exfoliated LAPONITE® nanodisks followed by anaerobic oxidation by the water protons, leading to the formation of the LAPONITE®-"decorated" Fe_3O_4 nanohybrids.

The structural, morphological, and physicochemical characteristics of the obtained nanohybrids with tunable magnetic loadings that varied from 25 to 95 wt% are given in the (ESI†). In particular, the overall properties concerning the material with 50 wt% Fe_3O_4 composition has been selectively shown in Fig. 1. The crystal structure of the LAPONITE®-"decorated" Fe_3O_4 nanoparticles was evaluated by combining the powder X-Ray diffraction pattern (XRD) and Mössbauer spectroscopy. The XRD pattern in Fig. 1(a) corresponds well to the $FeFe_2O_4$ pattern (JCPDS card no. #19-0629) for bulk magnetite, confirming the high crystalline nature of the material. The crystallite size of pure Fe_3O_4 nanoparticles estimated by the Scherrer equation on the highest intension diffraction peak (311) is

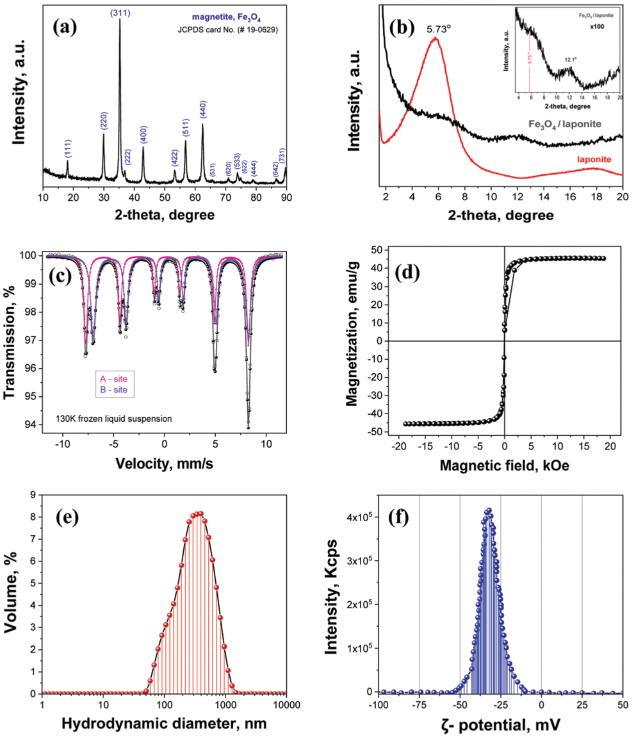

Fig. 1 Powder XRD patterns (a and b), Mössbauer spectra (c), room temperature magnetic hysteresis loops (d), hydrodynamic diameter distribution histogram (e), and ζ-potential distribution histogram (f) of the LAPONITE®-"decorated" Fe_3O_4 nanoparticle hybrids with 50 wt% Fe_3O_4 content.

about 19.3 nm. At the low angle area (Fig. 1(b)), the absence of the diffraction at $2\theta = 5.73°$, which corresponds to (001) crystal planes with a d spacing of 15.402 Å and refers to the layer spacing between the LAPONITE® platelets, indicates their successful exfoliation. However, with a magnification of over a hundred times (Fig. 1(b)/inset), the pattern of the hybrid nanomaterial shows the existence of very broad diffraction peaks at 2-theta degrees of about 6°, which corresponds to the interatomic space of d_{spacing} = 14.578 Å and 12° with d_{spacing} = 7.295 Å, respectively. This periodic pattern, which is obviously negligible, is probably due to the (001) and (002) lamellar LAPONITE® structure. Furthermore, XRD patterns of similar materials with 25, 75, 90, and 95 wt.% Fe_3O_4 nominal compositions are presented in the ESI† (Fig. S1(I)), which reveal similar structures regarding the iron oxide phase. The broad diffraction peaks, which are due to the LAPONITE® presence, are absent in samples with very high Fe_3O_4 content, as indicated by the low angle XRD patterns in Fig. S1(II), ESI† and are probably due to the composition effects and/or full exfoliation.

The ^{57}Fe Mössbauer spectrum of the frozen solution (colloid) of 50 wt% Fe_3O_4/LAPONITE® nanohybrid obtained at 130 K is given in Fig. 1(c). The spectrum shows two components with distinct peaks (sextets) and is very similar to the characteristic Mössbauer spectrum of pure magnetite with an inversed spinel structure. The outer sextet (pink in color) corresponds to the A-sites of Fe^{3+} ions in tetrahedral sites and the inner sextet (violet in color) correlates with the B-sites containing both Fe^{2+} and Fe^{3+} ions in octahedral sites. In the ^{57}Fe Mössbauer spectrum of Fig. 1(c), the fitted isomer shift for the A-sites was found to be equal to 0.33 mm s^{-1}, while that of the octahedral B-sites was 0.75 mm s^{-1}, the latter being an intermediate value resulting in electron hopping between the ferrous and ferric cations. The corresponding average hyperfine field, B_{hf}, was 495 KG for the A-sites and 482 KG for the B-sites. The latter value, combined with the characteristic isomer shift associated with the presence of divalent iron (Fe^{2+}) in the B-sites, matches the expected values for magnetite. In the case of pure magnetite, a relative A : B sextet area ratio of 1 : 2 is expected, reflecting the A : B site occupancy. For the ^{57}Fe Mössbauer spectrum, the fitted A : B area ratio obtained is 43 : 57. Assuming that the B component (57% of Fe) derives only from the B site, it indicates that an upper limit of 28% of the Fe of the A component can be attributed to magnetite. Thus, we calculate that 15% of the total Fe may be attributed to non-magnetite trivalent Fe oxides. This gives us an estimation of at least 85% of iron to be present in the form of magnetite. The higher A : B ratio value of 0.75 (= 43 : 57) compared to 0.50 (= 1/2) for the bulk inversed spinel ferrite, Fe_3O_4 structure is probably due to the superstoichiometry in oxygen or cationic vacancies.[66]

The magnetic properties of various Fe_3O_4/LAPONITE® hybrids were studied by a Vibrating Sample Magnetometer (*VSM*) at room temperature. The 50 wt% Fe_3O_4/LAPONITE® hybrid shows superparamagnetic behavior[10] with 45.4 emu g^{-1} magnetization at 2 Tesla, as evidenced from the room temperature magnetic hysteresis loop in Fig. 1(d). Similar magnetic behavior, with the saturation magnetization values ranging from 18 emu g^{-1} to 62 emu g^{-1} for various magnetic contents of 25 to 95 wt% Fe_3O_4/LAPONITE®; appeared in the whole studied Fe_3O_4/LAPONITE® powders regardless of the hybrid material composition. In particular, the saturation magnetization values of 25, 75, 90, and 95 wt% Fe_3O_4 contents are 18, 59.1, 61.1, and 62.2 emu g^{-1}, respectively, as indicated by the relative magnetization curve in Fig. S2 (ESI†). Considering the weight percentages of the diamagnetic clay matrix of LAPONITE® RD in each composite hybrid material, the saturation magnetization values, in particular, correspond to 72 emu g^{-1} (25 wt% Fe_3O_4), 90.8 emu g^{-1} (50 wt% Fe_3O_4), 78.8 emu g^{-1} (75 wt% Fe_3O_4), 67.9 emu g^{-1} (90 wt% Fe_3O_4), and 65.5 emu g^{-1} (95 wt% Fe_3O_4), respectively. The results show that the magnetization maximized in the sample with 50 wt% Fe_3O_4 content and reached a very high value, which is approaching the saturation magnetization of bulk magnetite (92 emu g^{-1}).[67,68]

The determination of the physicochemical properties of such materials is presented in Fig. 1(e) and (f) and in the ESI† (Fig. S3 and S4). The hydrodynamic diameter distribution given in Fig. 1(e) reveals a polydispersity with a mean diameter of 202.6 nm for the Fe_3O_4/LAPONITE® hybrids with 50 wt% content. This value is quite higher than the one corresponding to the pure LAPONITE® (80 nm in distilled water),[69] which is probably attributed to the formation of bridges between the LAPONITE® platelets. Furthermore, the electrokinetic

ζ-potential at the slipping plane of 50 wt% Fe_3O_4/LAPONITE®, shown in Fig. 1(f), indicates a high negative ζ-potential value of −31.6 mV, confirming the stability of the hybrids. Generally, ζ-potential values $>|30|$ mV denote adequate electrostatic repulsion to provide colloidal stability.[70] By varying the Fe_3O_4 content, the hydrodynamic mean diameter ranges from 136, 202.6, and 174 nm for the 25, 50, and 75 wt%, respectively, while the hybrid materials with higher Fe_3O_4 content (90 and 95 wt%) reveal multimodal size distribution as presented in Fig. S3 (ESI†). On the other hand, the ζ-potential values decrease as the Fe_3O_4 content increases. The corresponding values are −34.1 mV and −31.6 mV for compositions with 25 wt% and 50 wt% Fe_3O_4 and −22.3, −17.6, and −11.4 mV for those with 75, 90, and 95 wt% Fe_3O_4/LAPONITE®, as given in Fig. S4 (ESI†). This behavior is expected since the negative surface charge is originating from the nature of the LAPONITE® platelets, which shows that the hybrid materials with even a high magnetic loading up to 75% Fe_3O_4 content are stable and with excellent stability for the hybrids of 25 and 50 wt.% Fe_3O_4 composition.

The precise morphology of the nanomaterials was identified using the TEM studies. Representative TEM images at varied magnifications received from the 50 wt% Fe_3O_4 content hybrid material are selectively presented in Fig. 2, while the TEM images of the remaining compositions (25, 75, 90, and 95 wt.% Fe_3O_4) are shown in the ESI† (Fig. S5). At the lower Fe_3O_4 content (25 and 50 wt%), the nanoparticles possess a cuboidal shape, while by increasing the Fe_3O_4 content, the shape of the particles turns to multicore like (75 and 90 wt%, Fig. S5(d)–(f) and (g)–(i), ESI† respectively) and mostly irregular for the sample with the higher Fe_3O_4 content (95 wt%, Fig. S5(j) and (k)ESI†). Concerning the size of the cuboidal particles in the lowest Fe_3O_4 content sample (25 wt% Fe_3O_4) varying between 10–20 nm, the latter of which is slightly increased for the 50 wt% Fe_3O_4 content. Further increase in the Fe_3O_4 content seems to affect the size significantly and for the sample with higher than 75% Fe_3O_4 content in which the particles size is in the 60–80 nm range. Additional morphological characterization is also supported by atomic force microscopy images, presented in Fig. S6 (ESI†). The images originate from the 50 wt% Fe_3O_4 hybrid, and as it turns out, the material maintains the ability to create uniform films due to the layered nanoclay counterpart presence.

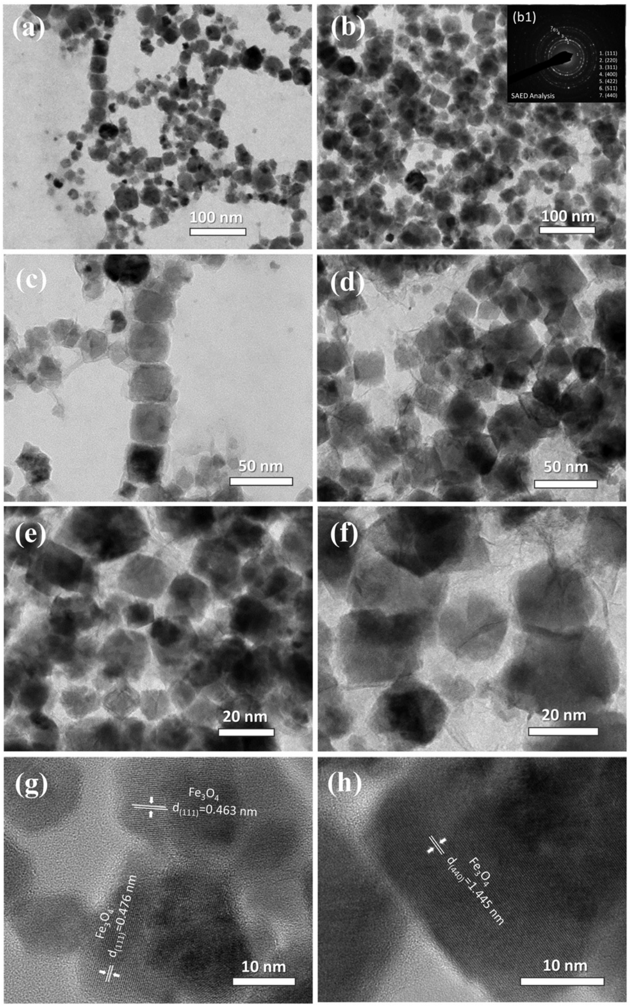

Fig. 2 Transmission electron microscopy (a)–(f) and high-resolution TEM (g) and (h) images with the corresponding selected area electron diffraction pattern (b1) from the LAPONITE®-"decorated" magnetite nanoparticles with 50 wt% Fe_3O_4 content.

The temperature profiles plotted as a function of time are presented in Fig. 3(a) and Fig. S7 in the ESI.† The best performance appeared for the case of 50 wt% Fe_3O_4 content (Fig. 3(b)). The colloidal solution temperature increased from 297.4 to 350.4 K (ΔT = 53 K) after 45 s of field exposure, displaying a rate of 1.18 °C s^{-1}, which is similar to the work of Lartigue *et al.*[71] in which the heating rate was 1.04 °C s^{-1}, under 29 kA m^{-1} and 520 kHz. To the best of our knowledge, these heating rates are the highest reported in the literature. Furthermore, we have to notice that in the present work, the heating rate is achieved by the use of an almost similar field (28 kA m^{-1}) but at a much lower frequency (150 kHz). As mentioned above, the most efficient sample is the 50 wt% Fe_3O_4 as shown in Fig. 3(b). Its SAR values under different concentrations ranging from 503 W g^{-1} (5.5. mg mL^{-1}) to 520 W g^{-1} (11.5. mg mL^{-1}) maximize and reach 540 W g^{-1} under concentrated conditions (22 mg mL^{-1}), while the magnetic content affects significantly the SAR values, which are in the range of 100–250 W g^{-1} from the lower to the higher magnetic content (Fig. 3(b)) and slightly varied with the colloid concentration. The maximization of the SAR values in the 50 wt% regime is connected with stability issues as well as size, morphology, and magnetic property issues.[72] In particular, the cuboidal nature of the Fe_3O_4 particles, which is obvious in the high resolution TEM images (Fig. 2(h) and (i)), together with the high net magnetization value (90.8 emu g^{-1} at 2 T), which is close to the bulk magnetite properties, and the successful decoration with the diamagnetic clay, which favors the suppression of the interparticle magnetic interactions is well known to enhance the T_2-weighted MRI contrast ability[69,73] and is probably responsible for the superior magnetic hyperthermia performance.[74]

Regarding iron oxide nanomaterials, the SAR values presented here are among the highest compared to the literature

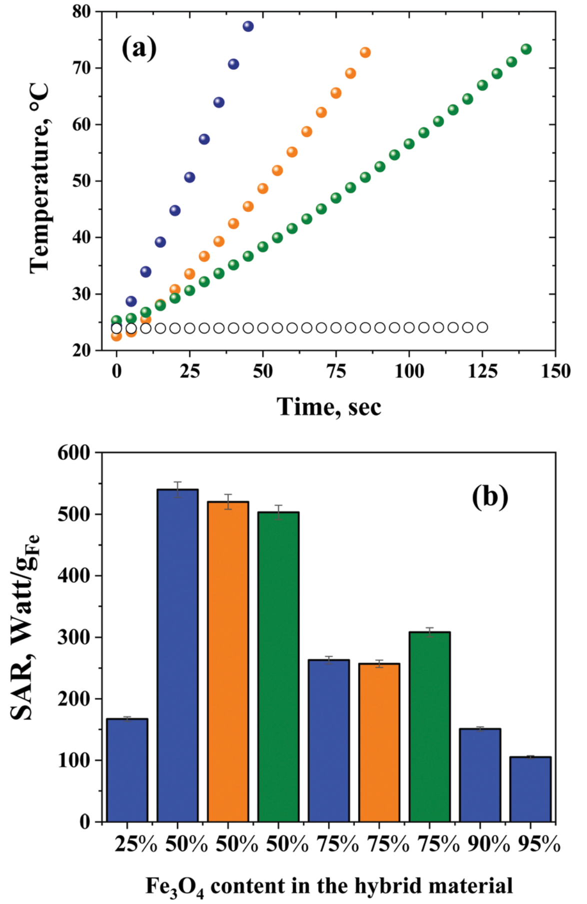

Fig. 3 Temperature profile as a function of the field exposure time (a) for the 50 wt% LAPONITE®-"decorated" Fe_3O_4 nanoparticle hybrids under different concentrations: 22 (blue), 11.5 (orange), and 5.5 (green) mg mL^{-1}, measured at 28 kA m^{-1} and 150 kHz. The open circles represent the control sample (distilled water). SAR values (b) of LAPONITE®-"decorated" Fe_3O_4 with variable Fe_3O_4 content (25–95 wt% Fe_3O_4/LAPONITE®), and solution concentration: 22 (blue), 11.5 (orange), and 5.5 (green) mg mL^{-1}.

(Table S1, ESI†) in terms of magnetic field and frequency conditions and are comparable or even better than the iron oxide cubes,[50,75] rods,[20] tubes, rings/hollow,[49] multicores,[71] assemblies,[76,77] branched,[72] and cube assemblies,[23] which have been recently reported. Among them, some materials reveal extremely high SAR values, in the order of a few thousand W g^{-1}, but we have to notice, taking into consideration the linear dependence with the frequency[52,78] that this is mainly due to the very high frequency up to 700 kHz. In addition, it should be noted that these frequencies are much higher than the recommended frequency for human exposure (lower than 200 kHz).[53]

Cell toxicity studies (no alternating magnetic field (AMF)) revealed no difference in toxicity in human GBM and fibroblast cell survival and proliferation 48 h after treatment with the LAPONITE®-"decorated" Fe_3O_4 nanoparticles (Fig. 4) in comparison to the control untreated cells. A large drop in GBM cell survival and proliferation was found in both multiple epidermal growth factor receptor (EGFR) – expressing and therapy-resistant GBM cell lines after application of AMFs and thermotherapy for 10 min at a low frequency (Fig. 5).

The LAPONITE®-"decorated" Fe_3O_4 nanoparticles predominantly affected the transverse T_2 relaxation time of tissue water that resulted in a signal drop on MRI T_2-weighted imaging, allowing for imaging of the MNPs (Fig. 6). Deposition of the nanoparticles was found in the brain after CED on day 0 that persisted 7 days after CED.

Conclusions

Highly crystalline superparamagnetic Fe_3O_4 nanoparticles "decorated" by LAPONITE® clay platelets have been successfully fabricated following a facile chemical approach, in multi grams scale, utilizing the Schikorr reaction, which involves the oxidation of layered $Fe(OH)_2$. The hybrid materials show excellent, long-term physicochemical stability in water due to their electrostatic repulsions and excellent heat induction properties, exhibiting a large SAR value of 540 W g^{-1} at a very low frequency (150 kHz), which can be attributed to the high magnetization value, and the suppression of the magnetic

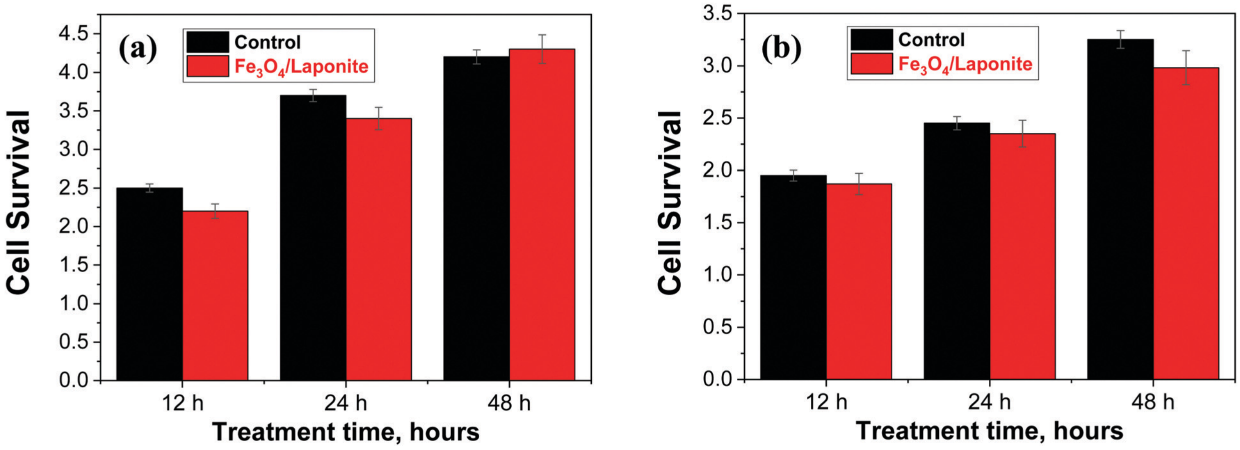

Fig. 4 Cell toxicity (without AFM field) in GBM cells (U87-EGFRvIII) (a) and human fibroblasts (HFF1) (b). The Fe_3O_4/LAPONITE® hybrid concentration is 3 mg mL^{-1}.

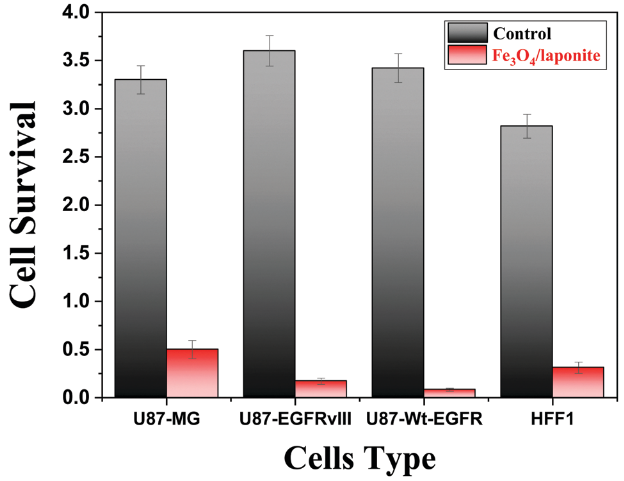

Fig. 5 Hyperthermia generation and GBM antitumor effect of the LAPONITE®-"decorated" Fe_3O_4 nanoparticles. The Fe_3O_4/LAPONITE® hybrid concentration is 3 mg mL^{-1}. U87-MG, U87-EGFRvIII, and U87wtEGFR GBM cells were treated at a low AMF dose (150 kHz) for 10 min.

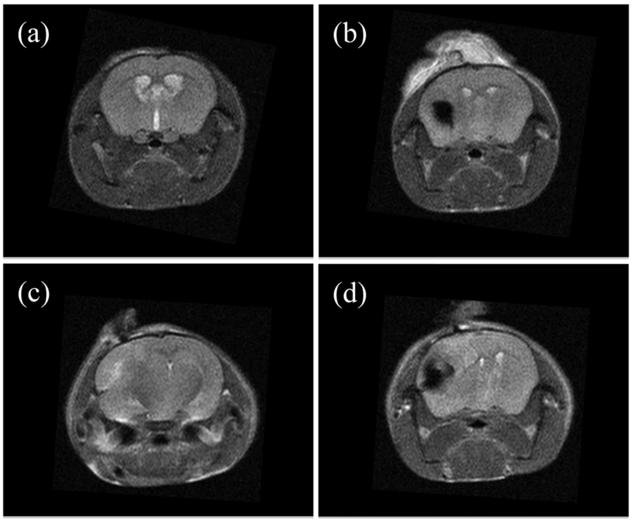

Fig. 6 T_2-weighted MR imaging of the rodent brain after convection-enhanced delivery (CED) of the LAPONITE®-"decorated" Fe_3O_4 nanoparticles. A: MR imaging of the brain (top) on day 0 with HBSS (a left) and MNPs (b right). B: MR imaging 7 days (down) after CED of HBSS (c left) and MNPs (d right).

interactions owing to the capping of Fe_3O_4 nanoparticles by the diamagnetic LAPONITE® nanodisks. Furthermore, the composite materials reveal excellent biocompatibility with minimal to no toxicity effect in therapy resistant GBM or HFF cells at 12, 24, and 48 h of treatment with the LAPONITE®-"decorated" Fe_3O_4 in comparison to the control treatment of cells. The application of a low dose AMF, however, produced a large antitumor effect in multiple EGFR-expressing human GBM cell lines due to the generation of local hyperthermia. In MR imaging, the materials provide excellent contrast generation in the rodent brain while at the same time serving as a promising nontoxic biocompatible magnetic platform that can be used for effective magnetic hyperthermia applications.

This nontoxic and facile magnetic platform can be additionally an excellent candidate for various practical fields, including ferrofluid technologies and magnetic sorbents.

Experimental

Materials and methods

Reagents and materials. Ferrous acetate and ammonia 25% solution were purchased from Sigma-Aldrich, while LAPONITE® RD was kindly provided by Rockwood, Clay additives GmbH, and consists of colloidal disks with a diameter of 30 ± 5 nm and a thickness of about 1 nm.

The reaction was carried out under as much anaerobic conditions as possible, titrating $Fe(OH)_2$ by exfoliated LAPONITE® platelets followed by oxidation according to Schikorr reaction (reaction (1))[79,80] in contrast to our previous work[69] in which exfoliated LAPONITE® platelets were decorated with $Fe(OH)_2$ followed by dehydration and condensation reactions. Briefly, the procedure is based on the oxidation of $Fe(OH)_2$ by the water protons under anaerobic conditions according to the following reaction.

$$3Fe(OH)_2 \rightarrow Fe_3O_4 + H_2 + 2H_2O \quad (1)$$

During the synthesis process, the formation of $Fe(OH)_2$ was achieved by ammonia precipitation of ferrous ions (Ferrous acetate) in a well degassed (applying a high vacuum) aqueous solution under continuous nitrogen gas bubbling at 60–80 °C. Subsequently, the deep olive-green $Fe(OH)_2$ dispersion was titrated by the dropwise addition of a well exfoliated, 1 wt% LAPONITE® RD water solution when the anionic LAPONITE® species were readily adsorbed on the positively charged surface of $Fe(OH)_2$, resulting in the formation of a layered composite. Finally, the olive-green composite material of layered LAPONITE®/$Fe(OH)_2$ was turned into a crude black hybrid material consisting of LAPONITE® platelets "decorated" by Fe_3O_4 nanoparticles. It is worth mentioning that the dark olive color is due to the partial oxidation of Fe^{2+} ions owing to the presence of the low amount of dissolved oxygen, which still remains even after extensive degassing with nitrogen bubbling.

Characterization of the Fe_3O_4/LAPONITE® nanohybrids. The crystal structure of the materials was determined by powder X-ray diffraction (Rigaku Ultima IV) with CuKα radiation. Mössbauer spectra were collected using a conventional transmission spectrometer with a ^{57}Co(Rh) source moving with constant acceleration at RT. Isomer shifts are given with respect to metallic iron at RT. Mössbauer spectra were least squares fitted using the IMSG program 85. The size and the morphology of the particles were analyzed using transmission electron microscopy (TEM, JEOL JEM-3010), and the magnetic properties were measured with a 2T vibrating sample magnetometer (VSM, Quantum Design). Electrophoretic measurements based on laser Doppler velocimetry and dynamic light scattering (DLS) were accomplished with a Malvern Instruments Nano

ZetaSizer at pH = 6.5. Magnetic hyperthermia measurements were performed on distilled water dispersions in which the nanomaterial concentrations ranged from 5–22 mg mL^{-1}, exposed to a radio frequency (RF) electromagnetic field of 28 kA m^{-1} under the frequency of 150 kHz. The SAR values, in Watts per iron g, were calculated by using the initial slopes ($\Delta T/\Delta t$, *i.e.* heating rates) of the temperature–time curves of Fig. 3(a). The temperature was recorded with an alcohol thermometer with 0.1 °C precision. Overall, the temperature measurement error was estimated at 0.3 °C. The error of the time measurements was at 0.5 s. The resulting SAR values have been calculated with an error of 5 Watt g_{Fe}^{-1}. The exact Fe concentration was estimated by atomic absorption spectroscopy, AAS.

Toxicity and GBM cell studies. Toxicity studies were performed with human glioblastoma (GBM) cells (U87EGFRvIII) and human foreskin fibroblasts (HFF) after treatment with the LAPONITE®-"decorated" Fe_3O_4 nanoparticles (12, 24, and 48 h) or control (medium) and without an alternating magnetic field. Therapy resistant human GBM cells (U87wtEGFR and U87EGFRvIII) that overexpress the wildtype-epidermal growth factor receptor (wt-EGFR) or the deletion mutant EGFRvIII, were treated with the LAPONITE®-"decorated" Fe_3O_4 nanoparticles (3 mg mL^{-1} in the composite material) or control (medium). After 24 h of incubation with the LAPONITE®-"decorated" Fe_3O_4 nanoparticles, GBM cells were treated with an AMF (150 kHz) for 10 min. Glioblastoma cells (U87MG and U87ΔEGFRvIII) and HFF cells were seeded in triplicate in 48-well flat-bottomed plates (80 000 cells per well) and incubated overnight at 37 °C. Confluent monolayers of cells were washed with PBS and then incubated with control (PBS) or the LAPONITE®-"decorated" Fe_3O_4 nanoparticles (3 mg mL^{-1} in the composite material) for 1 h at 37 °C. Cells were then washed with PBS to remove the nanoparticles and placed back in the incubator after the addition of medium. The crystal violet assay was performed at 12, 24, and 48 h to determine cell proliferation and survival. Absorbance measurements were performed on a microtiter plate reader at a wavelength of 570 nm. Absorbance values are presented as the mean of three wells per treatment.

***In vivo* MR imaging Ssudies.** Iron oxide nanoparticles (IONPs) have unique magnetic properties, which generate significant transverse T_2 relaxation time shortening and susceptibility effects resulting in strong T_2 weighted contrast on MRI.[81,82] A total of 3 athymic nude mice underwent convection-enhanced delivery (CED) of the LAPONITE®-"decorated" Fe_3O_4 nanoparticles (3 mg mL^{-1}) or Hanks' Balanced Salt Solution (HBSS; Gib-co Invitrogen Life Technologies, Inc., Grand Island, NY) at a rate of 0.5 μL min^{-1} for 20 min (total of 10 μL). The infusion apparatus consisted of a hydraulic drive serially connected to a digital syringe pump controller described previously (UltraMicroPumpII, World Precision Instruments, Inc., Sarasota, Florida).[83,84] The digital controller was able to precisely dispense microliter volumes at a set rate (μL min^{-1}) from up to three hydraulic drives simultaneously. Each hydraulic drive depressed the plunger of a gas-tight 50 μL Hamilton syringe fitted with 30-gauge removable needle (Hamilton Co., Reno, Nevada). A mounting bar was then used to mount the hydraulic drive and Hamilton syringe to up to three small animal stereotaxic instruments (David Kopf Instruments, Tujunga, CA). After infusion completion, the cannula needle was left in place for 5 min and then withdrawn at a rate of 1 mm min^{-1} to minimize any infuscate leakback. Animals underwent CED of MNPs (N = 3 HBSS and N = 3 LAPONITE®-"decorated" Fe_3O_4 nanoparticles) as described above. These athymic nude mice were scanned on a 4.7 T animal MRI scanner using a dedicated mouse coil (Varian Unity) on days 0 and 7 after CED using a dedicated rodent coil. Animals were anesthetized using 2% isofluorene gas and kept warm with a heated pad during the scan. T_2 weighted fast spin echo sequences with TR/TE = 6500/70 ms were typically used for imaging of the tumor and MNPs in the brain. Axial images were collected in a field of view of 2 cm, matrix of 256,[85] slice thickness of 1 mm, and a total of 11 slices to cover the entire brain region.

Author contributions

G. B., and V. T. designed and performed the materials synthesis concept for targeted biomedical applications and did the paper writing. *In vitro* magnetic hyperthermia experiments were performed by G. B. and G. D. while cell toxicity, hyperthermia, and T_2 weighted MR imaging were performed by A. B., and C. H. XRD studies were performed by V. P., and G. B. Magnetic characterization was performed by G. H, M. P. and G. B. while Mössbauer spectroscopy was performed by E. D. TEM and DLS studies were performed by S. A., G. B., and A. T. All authors have given approval to the final version of the manuscript.

Conflicts of interest

There are no conflicts to declare.

Notes and references

1 J. Frenkel and J. Doefman, *Nature*, 1930, **126**, 274–275.
2 D. Peddis, S. Laureti and D. Fiorani, *New Trends in Nanoparticle Magnetism*, Springer International Publishing, Cham, 2021.
3 M. Hu, H.-J. Butt, K. Landfester, M. B. Bannwarth, S. Wooh and H. Thérien-Aubin, *ACS Nano*, 2019, **13**, 3015–3022.
4 A. Barman, S. Mondal, S. Sahoo and A. De, *J. Appl. Phys.*, 2020, **128**, 170901.
5 E. Y. Vedmedenko, R. K. Kawakami, D. D. Sheka, P. Gambardella, A. Kirilyuk, A. Hirohata, C. Binek, O. Chubykalo-Fesenko, S. Sanvito, B. J. Kirby, J. Grollier, K. Everschor-Sitte, T. Kampfrath, C. Y. You and A. Berger, *J. Phys. D: Appl. Phys.*, 2020, **53**, 453001.
6 G. C. Lavorato, R. Das, J. Alonso Masa, M.-H. Phan and H. Srikanth, *Nanoscale Adv.*, 2021, **3**, 867–888.

7 K. Zhu, Y. Ju, J. Xu, Z. Yang, S. Gao and Y. Hou, *Acc. Chem. Res.*, 2018, **51**, 404–413.

8 G. Basina, I. Panagiotopoulos, E. Devlin, G. Hadjipanayis, L. Colak, C. Hadjipanayis, H. Mao, G. Diamantopoulos, M. Fardis, G. Papavasileiou, D. Niarchos and V. Tzitzios, *MRS Online Proc. Libr.*, 2010, **1256**, 635.

9 I. Yildiz, *Nanotechnol. Rev.*, 2016, **5**, 331–340.

10 A. V. Samrot, C. S. Sahithya, J. Selvarani, A. S.-K. Purayil and P. Ponnaiah, *Curr. Res. Green Sustainable Chem.*, 2021, **4**, 100042.

11 S. Zhao, X. Yu, Y. Qian, W. Chen and J. Shen, *Theranostics*, 2020, **10**, 6278–6309.

12 Y. Hu, S. Mignani, J.-P. Majoral, M. Shen and X. Shi, *Chem. Soc. Rev.*, 2018, **47**, 1874–1900.

13 G. Basina, V. Tzitzios, D. Niarchos, W. Li, H. Khurshid, H. Mao, C. Hadjipanayis and G. Hadjipanayis, *AIP Conf. Proc.*, 2010, **1311**, 441–446.

14 K. C. Barick, M. Aslam, Y.-P. Lin, D. Bahadur, P. V. Prasad and V. P. Dravid, *J. Mater. Chem.*, 2009, **19**, 7023–7029.

15 J. Huang, L. Bu, J. Xie, K. Chen, Z. Cheng, X. Li and X. Chen, *ACS Nano*, 2010, **4**, 7151–7160.

16 C. Lu, L. Han, J. Wang, J. Wan, G. Song and J. Rao, *Chem. Soc. Rev.*, 2021, **50**, 8102–8146.

17 Y. Bao, J. A. Sherwood and Z. Sun, *J. Mater. Chem. C*, 2018, **6**, 1280–1290.

18 H. Li, S. Yang, D. Hui and R. Hong, *Nanotechnol. Rev.*, 2020, **9**, 1265–1283.

19 G. Diamantopoulos, G. Basina, V. Tzitzios, E. Karakosta, M. Fardis, Z. Jaglicic, N. Lazaridis and G. Papavassiliou, *J. Magn. Magn. Mater.*, 2013, **336**, 71–74.

20 R. Das, J. Alonso, Z. Nemati Porshokouh, V. Kalappattil, D. Torres, M.-H. Phan, E. Garaio, J. Á. García, J. L. Sanchez Llamazares and H. Srikanth, *J. Phys. Chem. C*, 2016, **120**, 10086–10093.

21 Y. Lv, Y. Yang, J. Fang, H. Zhang, E. Peng, X. Liu, W. Xiao and J. Ding, *RSC Adv.*, 2015, **5**, 76764–76771.

22 S. Pourmiri, V. Tzitzios, G. C. Hadjipanayis, B. P. Meneses Brassea and A. A. El-Gendy, *AIP Adv.*, 2019, **9**, 125033.

23 D. Niculaes, A. Lak, G. C. Anyfantis, S. Marras, O. Laslett, S. K. Avugadda, M. Cassani, D. Serantes, O. Hovorka, R. Chantrell and T. Pellegrino, *ACS Nano*, 2017, **11**, 12121–12133.

24 A. Muela, D. Muñoz, R. Martín-Rodríguez, I. Orue, E. Garaio, A. Abad Díaz de Cerio, J. Alonso, J. Á. García and M. L. Fdez-Gubieda, *J. Phys. Chem. C*, 2016, **120**, 24437–24448.

25 W. Guo, C. Yang, H. Lin and F. Qu, *Dalton Trans.*, 2014, **43**, 18056–18065.

26 G. Basina, G. Mountrichas, E. Devlin, N. Boukos, D. Niarchos, D. Petridis, S. Pispas and V. Tzitzios, *J. Nanosci. Nanotechnol.*, 2009, **9**, 4753–4759.

27 H. Song, F. Quan, Z. Yu, M. Zheng, Y. Ma, H. Xiao and F. Ding, *J. Mater. Chem. B*, 2019, **7**, 433–442.

28 K.-k Xia, Y. Lyu, W.-t Yuan, G.-x Wang, H. Stratton, S.-j Zhang and J. Wu, *Front. Oncol.*, 2019, **9**, 250.

29 M. Shao, F. Ning, J. Zhao, M. Wei, D. G. Evans and X. Duan, *J. Am. Chem. Soc.*, 2012, **134**, 1071–1077.

30 F. Soetaert, P. Korangath, D. Serantes, S. Fiering and R. Ivkov, *Adv. Drug Delivery Rev.*, 2020, **163-164**, 65–83.

31 M. Usman, J. M. Byrne, A. Chaudhary, S. Orsetti, K. Hanna, C. Ruby, A. Kappler and S. B. Haderlein, *Chem. Rev.*, 2018, **118**, 3251–3304.

32 L. Hao, M. Liu, N. Wang and G. Li, *RSC Adv.*, 2018, **8**, 39545–39560.

33 R. S. Bangari, V. K. Yadav, J. K. Singh and N. Sinha, *ACS Omega*, 2020, **5**, 10301–10314.

34 T. Yavuz Cafer, J. T. Mayo, W. Yu William, A. Prakash, C. Falkner Joshua, S. Yean, L. Cong, J. Shipley Heather, A. Kan, M. Tomson, D. Natelson and L. Colvin Vicki, *Science*, 2006, **314**, 964–967.

35 W. F. Elmobarak and F. Almomani, *Chemosphere*, 2021, **265**, 129054.

36 Y. F. Shen, J. Tang, Z. H. Nie, Y. D. Wang, Y. Ren and L. Zuo, *Sep. Purif. Technol.*, 2009, **68**, 312–319.

37 J. Yoo, N. Park, J. H. Park, J. H. Park, S. Kang, S. M. Lee, H. J. Kim, H. Jo, J.-G. Park and S. U. Son, *ACS Catal.*, 2015, **5**, 350–355.

38 G. Basina, O. Elmutasim, D. A. Gaber, S. A. Gaber, X. Lu, V. Tzitzios, B. V. Vaithilingam, M. Baikousi, G. Asimakopoulos, M. A. Karakassides, I. Panagiotopoulos, K. Spyrou, E. Thomou, E. Sakellis, N. Boukos, D. Xu, M. Tsapatsis, N. A. Amoodi and Y. A. Wahedi, *Appl. Catal., B*, 2020, **278**, 119338.

39 N. Thomas, D. D. Dionysiou and S. C. Pillai, *J. Hazard. Mater.*, 2021, **404**, 124082.

40 J. Wei, R. Yao, Q. Ge, Z. Wen, X. Ji, C. Fang, J. Zhang, H. Xu and J. Sun, *ACS Catal.*, 2018, **8**, 9958–9967.

41 A. V. Nikam, B. L.-V. Prasad and A. A. Kulkarni, *CrystEngComm*, 2018, **20**, 5091–5107.

42 V. K. Tzitzios, A. Bakandritsos, V. Georgakilas, G. Basina, N. Boukos, A. B. Bourlinos, D. Niarchos and D. Petridis, *J. Nanosci. Nanotechnol.*, 2007, **7**, 2753–2757.

43 V. Tzitzios, V. Georgakilas, I. Zafiropoulou, N. Boukos, G. Basina, D. Niarchos and D. Petridis, *J. Nanosci. Nanotechnol.*, 2008, **8**, 3117–3122.

44 G. Basina, H. Khurshid, N. Tzitzios, G. Hadjipanayis and V. Tzitzios, *Nanomaterials*, 2021, **11**, 1141.

45 G. F. Baronzio and E. D. Hager, *Hyperthermia in cancer treatment: a primer*, Landes Bioscience/Eurekah.com, Springer Science + Business Media, Georgetown, Tex., New York, N.Y, 2006.

46 R. K. Gilchrist, R. Medal, W. D. Shorey, R. C. Hanselman, J. C. Parrott and C. B. Taylor, *Ann. Surg.*, 1957, **146**, 596–606.

47 J.-P. Fortin, C. Wilhelm, J. Servais, C. Ménager, J.-C. Bacri and F. Gazeau, *J. Am. Chem. Soc.*, 2007, **129**, 2628–2635.

48 L. Storozhuk, M. O. Besenhard, S. Mourdikoudis, A. P. LaGrow, M. R. Lees, L. D. Tung, A. Gavriilidis and N. T.-K. Thanh, *ACS Appl. Mater. Interfaces*, 2021, **13**, 45870–45880.

49 G. Niraula, J. A.-H. Coaquira, G. Zoppellaro, B. M.-G. Villar, F. Garcia, A. F. Bakuzis, J. P.-F. Longo, M. C. Rodrigues, D. Muraca, A. I. Ayesh, F. S.-M. Sinfrônio, A. S. de Menezes, G. F. Goya and S. K. Sharma, *ACS Appl. Nano Mater.*, 2021, **4**, 3148–3158.

50 P. Guardia, R. Di Corato, L. Lartigue, C. Wilhelm, A. Espinosa, M. Garcia-Hernandez, F. Gazeau, L. Manna and T. Pellegrino, *ACS Nano*, 2012, **6**, 3080–3091.

51 Y. Yang, M. Huang, J. Qian, D. Gao and X. Liang, *Sci. Rep.*, 2020, **10**, 8331.

52 D. Kouzoudis, G. Samourgkanidis, A. Kolokithas-Ntoukas, G. Zoppellaro and K. Spiliotopoulos, *Front. Mater.*, 2021, **8**, 638019.

53 W. J. Atkinson, I. A. Brezovich and D. P. Chakraborty, *IEEE Trans. Biomed. Eng.*, 1984, **BME-31**, 70–75.

54 H. Huang, W. Feng and Y. Chen, *Chem. Soc. Rev.*, 2021, **50**, 11381–11485.

55 Y. Chen, C. Tan, H. Zhang and L. Wang, *Chem. Soc. Rev.*, 2015, **44**, 2681–2701.

56 R. Kumar, A. Chauhan, S. K. Jha and B. K. Kuanr, *J. Mater. Chem. B*, 2018, **6**, 5385–5399.

57 V. Karthika, M. S. AlSalhi, S. Devanesan, K. Gopinath, A. Arumugam and M. Govindarajan, *Sci. Rep.*, 2020, **10**, 18912.

58 E. P. Komarala, S. Nigam, M. Aslam and D. Bahadur, *New J. Chem.*, 2016, **40**, 423–433.

59 C. Prasad, H. Tang and W. Liu, *J. Nanostruct. Chem.*, 2018, **8**, 393–412.

60 G. R. Mahdavinia, M. Soleymani, H. Etemadi, M. Sabzi and Z. Atlasi, *Int. J. Biol. Macromol.*, 2018, **107**, 719–729.

61 G. R. Mahdavinia, S. Ettehadi, M. Amini and M. Sabzi, *RSC Adv.*, 2015, **5**, 44516–44523.

62 O. Goncharuk, Y. Samchenko, L. Kernosenko, O. Korotych, T. Poltoratska, N. Pasmurtseva, O. Oranska, D. Sternik and I. Mamyshev, *Soft Matter*, 2020, **16**, 5689–5701.

63 S. Xiao, R. Castro, D. Maciel, M. Gonçalves, X. Shi, J. Rodrigues and H. Tomás, *Mater. Sci. Eng., C*, 2016, **60**, 348–356.

64 L. Ding, R. Wang, Y. Hu, F. Xu, N. Zhang, X. Cao, X. Wang, X. Shi and R. Guo, *Appl. Clay Sci.*, 2020, **186**, 105447.

65 M. Liu, J. Zhang, X. Li, C. Cai, X. Cao, X. Shi and R. Guo, *J. Mater. Chem. B*, 2019, **7**, 3856–3864.

66 T. J. Daou, G. Pourroy, S. Bégin-Colin, J. M. Grenèche, C. Ulhaq-Bouillet, P. Legaré, P. Bernhardt, C. Leuvrey and G. Rogez, *Chem. Mater.*, 2006, **18**, 4399–4404.

67 P. Hu, T. Chang, W.-J. Chen, J. Deng, S.-L. Li, Y.-G. Zuo, L. Kang, F. Yang, M. Hostetter and A. A. Volinsky, *J. Alloys Compd.*, 2019, **773**, 605–611.

68 S.-W. Cao, Y.-J. Zhu and J. Chang, *New J. Chem.*, 2008, **32**, 1526–1530.

69 V. Tzitzios, G. Basina, A. Bakandritsos, C. G. Hadjipanayis, H. Mao, D. Niarchos, G. C. Hadjipanayis, J. Tucek and R. Zboril, *J. Mater. Chem.*, 2010, **20**, 5418–5428.

70 R. Greenwood, *Adv. Colloid Interface Sci.*, 2003, **106**, 55–81.

71 L. Lartigue, P. Hugounenq, D. Alloyeau, S. P. Clarke, M. Lévy, J.-C. Bacri, R. Bazzi, D. F. Brougham, C. Wilhelm and F. Gazeau, *ACS Nano*, 2012, **6**, 10935–10949.

72 N. H. AbuTalib, A. P. LaGrow, M. O. Besenhard, O. Bondarchuk, A. Sergides, S. Famiani, L. P. Ferreira, M. M. Cruz, A. Gavriilidis and N. T.-K. Thanh, *CrystEngComm*, 2021, **23**, 550–561.

73 L. Ding, Y. Hu, Y. Luo, J. Zhu, Y. Wu, Z. Yu, X. Cao, C. Peng, X. Shi and R. Guo, *Biomater. Sci.*, 2016, **4**, 474–482.

74 I. Castellanos-Rubio, O. Arriortua, D. Iglesias-Rojas, A. Barón, I. Rodrigo, L. Marcano, J. S. Garitaonandia, I. Orue, M. L. Fdez-Gubieda and M. Insausti, *Chem. Mater.*, 2021, **33**, 8693–8704.

75 L. Lartigue, C. Innocenti, T. Kalaivani, A. Awwad, M.-d M. Sanchez Duque, Y. Guari, J. Larionova, C. Guérin, J.-L. G. Montero, V. Barragan-Montero, P. Arosio, A. Lascialfari, D. Gatteschi and C. Sangregorio, *J. Am. Chem. Soc.*, 2011, **133**, 10459–10472.

76 D. Sakellari, K. Brintakis, A. Kostopoulou, E. Myrovali, K. Simeonidis, A. Lappas and M. Angelakeris, *Mater. Sci. Eng., C*, 2016, **58**, 187–193.

77 M. Jeong, S. Lee, D. Y. Song, S. Kang, T.-H. Shin and J.-s Choi, *ACS Omega*, 2021, **6**, 31161–31167.

78 R. E. Rosensweig, *J. Magn. Magn. Mater.*, 2002, **252**, 370–374.

79 G. Schikorr, *Z. Elektrochem. Angew. Phys. Chem.*, 1929, **35**, 65–70.

80 M. Ma, Y. Zhang, Z. Guo and N. Gu, *Nanoscale Res. Lett.*, 2013, **8**, 16.

81 J. W.-M. Bulte and D. L. Kraitchman, *NMR Biomed.*, 2004, **17**, 484–499.

82 C. G. Hadjipanayis, R. Machaidze, M. Kaluzova, L. Wang, A. J. Schuette, H. Chen, X. Wu and H. Mao, *Cancer Res.*, 2010, **70**, 6303–6312.

83 C. G. Hadjipanayis, W. Fellows-Mayle and N. A. Deluca, *Mol. Ther.*, 2008, **16**, 1783–1788.

84 A. I. Brooks, M. W. Halterman, C. A. Chadwick, B. L. Davidson, M. Haak-Frendscho, C. Radel, C. Porter and H. J. Federoff, *J. Neurosci. Methods*, 1998, **80**, 137–147.

85 B. Peng, X. Zhang, D. G.-A. L. Aarts and R. P.-A. Dullens, *Nat. Nanotechnol.*, 2018, **13**, 478–482.